https://doi.org/10.1016/j.conbuildmat.2021.125304

DEBONDING SIMULATION OF FIBRE-MATRIX INTERFACES OF FRP COMPOSITES WITH REACTIVE FORCE FIELD

Kui Lin and Tao Yu*

Department of Civil and Environmental Engineering,
The Hong Kong Polytechnic University, Hong Kong, China. Email: tao-cee.yu@polyu.edu.hk

Abstract: This paper presents a study on all-atom molecular dynamics (MD) simulations of fibre-matrix interfaces in fibre-reinforced polymer (FRP) composites, with a focus on the effect of fibre sizing. The reactive force field ReaxFF was used in the simulations. The sizing treatment was found to significantly increase the interface toughness while has little effect on the peak stress of fibre-matrix interface. The characteristics of the fracture surfaces and the scission of C-O bonds observed in the simulations are consistent with pervious experimental observations. The developed modelling method opens up a new avenue of investigating the deterioration mechanism of FRP under combined mechanical-chemical-thermal actions.

Keywords: FRP; sizing; interface; debonding; MD simulations; reactive force field; mechanochemical process.

1. INTRODUCTION

Fibre-reinforced polymer (FRP) composites, consisting of continuous fibres embedded in a polymeric matrix, have emerged as a durable construction material in the past three decades [1-2]. The use of FRP composites for strengthening existing structures has become a mainstream technique [3-9], while their use for new construction is gaining increasing acceptance [10-15]. In an FRP composite, the properties of the fibre-matrix interfaces are critical for the force transfer among the fibres and the matrix [16]. Existing studies have shown that the deterioration of fibre-matrix interfaces, due to thermal cycles, moisture and other environmental actions, may have significant effects on the mechanical properties of the FRP composites [17-20].

The majority of the existing studies on the mechanical and durability properties of FRP have been based on macroscale experiments and/or modeling [21-25]. To account for the presence of defects (e.g., pores) and the crack development within the material/structure, some studies have adopted the mesoscale modelling approach (e.g., [26-27]). Such modeling, however, is still based on continuum mechanics and thus cannot be used to explore micromechanisms at the atomic/molecular level. In recent years, some researchers [28-33] have also adopted advanced experimental techniques for microscopic characterization [e.g., using scanning electron microscopy (SEM), transmission electron microscopy (TEM) or X-ray computed tomography (CT)] and elemental/chemical analysis [e.g., using Raman spectroscopy, Fourier transform infrared spectroscopy (FTIR), X-ray photoelectron spectroscopy (XPS)]. These studies have provided some new insights into the properties of FRP and the roles of fibre-matrix interfaces, but the experimental techniques still do not allow the dynamic morphological evolution and chemical changes to be observed *in situ* at the nanoscale.

As a nanoscale simulation method, molecular dynamics (MD) simulation has been widely used in physics, mechanics, chemistry, and biology to explore micromechanisms and for understanding of the dynamic process at the atomic/molecular level. The use of MD simulation on the mechanical and durability properties of FRP has also been explored by some recent studies. In particular, the debonding mechanism at fibre-matrix interfaces of FRP has been investigated by MD simulation of the tension and/or shear processes of the interfaces in various environments (e.g., dry, wet and salt environments) [34-40]. With the MD simulation, the fibre-matrix interaction at the atomic/molecular level can be captured, and the fundamental debonding mechanism can be revealed by examining the changes in the configuration and energy/forces of the interfaces [38-39, 41-42]. In addition, MD simulations have been used to simulate the integrity and mechanical properties of FRP-concrete interfaces under different conditions (e.g., conformational changes and detaching of epoxy resin on C-S-H surfaces in aggressive environments such as moisture [43], salt solution [44], and sulfate solution [45]).

The existing studies on the MD simulation of fibre-matrix interfaces of FRP have mostly only considered nonbonding interactions (i.e., van der Waals forces and hydrogen bonds) between the fibres and the matrix [37, 41-43]. Apparently, such a treatment cannot simulate the mechanism associated with the breakage of chemical bonds due to mechanical and/or environmental actions at the interfaces. Chemical bonds between the fibres and the matrix, however, generally exist in commercial FRP products due to the application of a sizing layer (e.g., with a silane coupling agent) on the fibre surfaces which reacts with both the fibres and the matrix, and thus improve the adhesion between them [46-49]. Indeed, the fibre sizing has seldom been considered in the MD simulation of the existing studies. To the best of the authors' knowledge, only Zhang et al. [50] built the sizing layer into their molecular interface model, but the model used the classical force field which assumes the bonds between atoms are unchanged and thus cannot simulate the formation or breaking of chemical bonds. The oversimplification of the existing studies in this important issue might be due to the complexity in the construction of a model with chemical bonds properly formed between the components, as well as the relatively high computational costs. To simulate chemical reactions, reactive force fields (e.g., REBO [51] and ReaxFF [52-53] force fields) are generally required.

Against the above background, this paper presents a study on all-atom simulations of fibre-matrix interfaces, in which the roles of van der Waals forces, hydrogen bonds, and chemical bonds at the interfaces are all duly considered. The ReaxFF MD simulations were performed on fibre-matrix interfaces with and without fibre sizing to investigate its effect on the interfacial behaviour. In the following sections, the construction of MD models and the use of them for the simulation of tension process at the fibre-matrix interfaces are first presented, followed by discussions of the simulation results.

2. MODELLING METHODS

The Large-scale Atomic/Molecular Massively Parallel Simulator (LAMMPS) [54] was used to perform MD simulations for construction of the models and the tension process at the fibre-matrix interfaces. Details of the simulation methods are provided in this section.

2.1. Construction of Models

Two models were constructed in this study, including an untreated fibre (i.e., without sizing)-matrix model and a sizing-treated fibre-matrix model. The construction process of the latter contained two steps: (1) grafting the sizing onto the fibre surface; (2) cross-linking of the polymer matrix and coupling of the matrix with the (grafted) fibre surface. For the former model, only the second step above was involved. Classical MD simulations were used with the consistent valence force field (CVFF) for both steps. Although this method cannot simulate the actual chemical reaction process, it allows chemical bonds between reactive atoms to be formed based on the distance between them [55-56], at a relatively low computational cost. Therefore, the models constructed using this method are adequate for the purpose of the present study which is focused on the simulation of the dynamic process of fibre-matrix interfaces under tension (i.e., debonding simulation); the method of debonding simulation is presented in the next section.

The CVFF adopted for construction of the models is based on ab initio calculations and experiments [57]. The total potential energy considered in the CVFF consists of two parts, namely, the bond energy E_{bond} and the nonbond energy E_{nonbond}; the detailed equations describing the two parts are given in Appendix A. The formation of chemical bonds between reactive sites is assumed to occur when their distance is less than 2.5 Å. The choice of this distance ensures that the initial bond forces arising during the process are not overly large while an adequate degree of coupling can be obtained [58]. The van der Waals interactions are calculated with a cutoff distance of 12 Å, and the electrostatic interactions are described by the Ewald method with a cutoff distance of 10 Å. These cutoff distances are large enough to describe the nonbonding interactions [59].

Silica (quartz) with a size of $16.5 \times 157.2 \times 86.5$ Å was selected to model the glass fibre [60]. The size of silica model in the present study was chosen based on similar existing studies and is on the higher end compared to other studies (e.g. [32], [34-35], [39-40]). Considering the presence of unsaturated oxygen on the silica surface, the surface was hydroxylated [61]. Silane is widely used as a coupling agent between glass fibres and polymers (i.e., fibre sizing) [46-47]. In this study, 64 3-aminopropyltriethoxysilane (APTES) molecules were directly grafted [62] onto the fibre surface. A total of 3200 diglycidyl ether of bisphenol A (DGEBA) (epoxy) and 1, 3-Phenylenediamine (mPDA) (curing agent) monomers were used to model the polymer matrix.

2.1.1. Modelling of silane grafting

The process of grafting silane onto a silica surface was modelled in two steps [63-64]: (1) hydrolysis of the silane (Figure 1a); (2) formation of chemical bonds between the hydrolyzed species and the silanol groups of the hydroxylated silica surface (Figure 1b). In the modelling process, the 64 silane molecules were uniformly grafted on the fibre surface with a coverage degree of 0.47 nm^{-2}.

2.1.2. Modelling of cross-linking of polymer matrix and its coupling with fibre surface

The 3200 DGEBA and mPDA monomers were randomly placed in the simulation box in a one-to-one manner, in which the silica was placed at the bottom. The cross-linking of polymer matrix (i.e., the coupling between DGEBA and mPDA monomers, see Figure 1c) was performed on the surface of silica with periodic boundary conditions in the y and z directions (i.e., parallel to the fibre-matrix interface, see Figure 2), so that a periodic cross-linked polymer matrix can cover the fibre surface and potential defects (e.g., warping and debonding) at the edge of the contact area between the matrix and the fibre can be largely avoided. Such a periodic model provides a desirable interface for further investigation of the debonding mechanism. The size of the epoxy model is sufficiently large for the micromechanics investigated and is on the higher end compared to other similar studies (e.g., [32-40]).

For the model with a sizing layer, the amine group on the silane can also form chemical bonds with the epoxy [i.e., between the diamine reaction site (blue circle) in the silane and the diepoxide reaction site (red circle) in the DGEBA monomer, see Figure 1d]; this coupling process was simulated simultaneously with the cross-linking of polymer matrix. Figure 3a illustrates the process of constructing the model of treated fibre-matrix interface, while Figure 3b shows a snapshot of part of the interface model after coupling. It is evident from Figure 3b that the contact between the matrix and the fibre is extremely good.

To form the desired periodic cross-linking models, two steps were taken and the NVT (constant number of atoms, volume and temperature) ensemble was used for both steps. In the first step, a virtual wall was used to compress the loose monomers in the x direction until the mass density of the matrix was close to 0.8 g/cm^3, which is not too small (i.e., the monomers not being too loose) but is still considerably smaller than that of a typical cured matrix (i.e., 1.17~1.38 g/cm^3) [65-67]. The temperature was controlled at 380 K in this step. In the second step, the virtual wall was removed and the cross-linking simulation was performed at a temperature of 380 K for 0.7 ns as the cross-linking becomes extremely slow afterwards. The resulting cross-linking degrees are 71.4% and 73.9% for the models with and without sizing treatment, respectively. The two values are sufficiently close for the two models to serve in a comparative study, and are both close to those reported in the existing experimental studies on DGEBA/mPDA polymer (e.g., [65]).

2.1.3. Relaxation of models

After the cross-linking processes, the two models were relaxed to reduce the stress concentration inside the matrix [68]. The relaxation of the models was performed with the NPT (constant number of atoms, pressure and temperature) ensemble for 0.5 ns, where the pressure in the y and z directions was controlled at 1 atm. In this process, the temperature gradually dropped from 420 K to 300 K within the first 24 ps and then remained at 300 K. The Nose´–Hoover thermostat [69-70] with a timestep of 0.5 fs was employed to regulate the temperature. The way that the temperature of the relaxation process was controlled is shown in Figures 4a and 4b. It should be noted that, instead of using the CVFF, the relaxation process for both models was simulated with the ReaxFF force field [71], which is consistent with the subsequent debonding simulation presented in detail in the next section.

2.3. Simulation of Debonding

The debonding at the fibre-matrix interfaces was simulated by a tension process. As the debonding process may involve the breakage of chemical bonds, especially for the sizing-treated fibre-matrix interface, the ReaxFF force field [71], which is a reactive force field, was used in the simulation. The total potential energy of the ReaxFF force field has a more complicated form than that of the classical force field or the CVFF, so that it can directly simulate the actual chemical reaction process. The equations describing the total potential energy of the ReaxFF force field as well as all the energy terms, which are functions of the bond order, are given in Appendix B. Each model in the present study contains about 125,000 atoms involving computations of over 90,000 core hours, which is a large system for reaction force field simulations and is even larger than most fibre-matrix interface models (e.g., [32-40]) used in classical MD which does not consider covalent bonds.

In the debonding simulation, the top region of the matrix was fixed (Figure 2). The middle region (unfixed part) was simulated with the NVE (constant number of atoms, volume and energy) ensemble and the temperature was controlled at 300 K with a timestep of 0.5 fs. The tensile velocity of the bottom region of the fibre, which moved as a rigid body, was 20 m/s.

During the simulation process, the viral stress (see Appendix C for the equation describing the viral stress tensor) [72] of the middle region of the matrix were recorded every 500 steps. The so-called true stress or Cauchy stress [72] of the matrix can then be obtained by statistically averaging the virial stress of the matrix in the middle region. The stress-time curve was filtered with a 30-point fast Fourier transform (FFT) smoothing to eliminate thermal noises.

3. RESULTS AND DISCUSSIONS

3.1. Mass Density of Matrix

The mass density of the matrix is an important parameter for the behaviour of fibre-matrix interfaces. For example, it is well known that the attractive force between two flat surfaces due to the van der Waals interaction is proportional to the atomic number density, and thus the mass density, of the two surfaces according to the Hamaker's constant [73]. In reality, the mass density of the matrix depends on many factors including the types of monomers (e.g., DGEBA and mPDA), the resin-curing agent (e.g., DGEBA-mPDA) ratio, the temperature, the degree of cross-linking as well as the distribution and sizes of nano or subnano voids inside the matrix. The mass density of the matrix in the two models presented above are reported and discussed here, while further investigation into the effect of mass density of matrix on the interfacial behaviour is beyond the scope of this paper.

Figures 4a and 4b show that the density of the cross-linked matrix in the two models first increased in the relaxation process due to the decreasing temperature, and then became nearly constant after 40 ps when the temperature had been made stable at 300 K. The mass density of the matrix after 40 ps is 1.28 g/cm^3 for that in the sizing-treated fibre-matrix model (degree of cross-linking: 71.4%) and is 1.29 g/cm^3 for that in the untreated fibre-matrix model (degree of cross-linking: 73.9%). The slight difference between the two values is believed to be due to the different degrees of cross-linking. It should be noted that these values are also close to the theoretical and experimental mass densities of DGEBA/mPDA reported in the existing studies (e.g., [61-62, 65]), demonstrating the validity of the modelling method in the present study.

3.2. Debonding Process of Untreated Fibre-Matrix Interface

The stress-displacement curve obtained from the MD simulation of the untreated fibre-matrix interface is shown in Figure 5a in which the stresses are calculated by statistically averaging the virial stresses of all atoms in the unfixed region (i.e., true stress, see Section 2.3), while the displacement is taken as the elongation of the matrix. Hereafter in this paper, the stress and the displacement refer to those calculated/taken in the same way unless otherwise specified. Four typical states (I-IV, marked on the curve in Figure 5a) in the debonding process of the untreated fibre-matrix interface are illustrated in Figures 5b-e, respectively.

State I refers to the state of peak stress. It is evident from Figure 5b that at State I, the matrix is still in good contact with the fibre. After State I, the matrix starts to become detached from the fibre surface with a decreasing stress until State II is reached at a displacement of 1.2 nm, which is the cutoff distance for nonbonding interactions (see Section 2.1). At State II, Figure 5c shows that a small portion of the matrix still adheres to the fibre surface, and there is still a small tensile force between the two. This is because some of the polymer chains on the surface of the matrix slip off from the main body by breaking the intermolecular interaction (van der Waals forces and hydrogen bonds) between these and other chains in the matrix, due to the adhesion between the fibre and the matrix. With the increase of displacement, an increasing number of the remaining polymer chains at the fibre surface are pulled back due to the limited slippage length of the chains. As a result, the stress generally decreases with the displacement in this process. Figure 5d shows that at State III, only a few polymer chains are still attached to the fibre, while Figure 5e shows that at State IV when the stress is zero at a displacement of around 4.7 nm, all polymer chains are detached, leaving only a very small number of residues (monomer molecules and free radicals) on the fibre surface.

With the stress-displacement curve (Figure 5a), the interfacial tensile strength (i.e., peak stress of the curve) and toughness (i.e., area under the curve) can be found to be 286.2 MPa and 0.26 J/m^2, respectively. In addition, the elastic modulus of the matrix may be found from the initial linear portion of the curve. At the initial stage, the displacement Δd comes only from the deformation of the matrix which is perfectly adhered to the fibre surface (i.e., no displacement at the interface). Considering also that periodic boundary conditions are applied in the two directions (y and z) parallel to the interface, the deformation of the matrix in the x direction can be considered to be uniform over a y-z plane. Therefore, the true strain $\varepsilon_{\mathrm{true}}$ of the matrix can be calculated by $\varepsilon_{\mathrm{true}} = \Delta d / L_0$, where L_0 is the initial length of the unfixed part of the matrix. The elastic modulus of the matrix can be calculated to be 4.39 GPa by $E_0 = \sigma_{\mathrm{true}} / \varepsilon_{\mathrm{true}}$ (Figure 5a), where σ_{true} is the true stress. This value (i.e., 4.39 GPa) falls in the range of the elastic modulus of DGEBA/mPDA matrices tested in the previous studies (i.e., from 3.30 GPa to 4.75 GPa, see Table 1) [44, 65-66, 74-76], but is on the higher side and appears to be higher than most reported experimental values. This is not a surprise considering that a high strain rate was adopted in the MD simulation and that the test values in the previous studies may have been negatively affected by random imperfections in the test materials which were not included in the MD models.

A comparison can be made between the interfacial toughness and the work of adhesion W_{12} which is defined as the reversible thermodynamic work required to separate the interface from the equilibrium state of two phases to a separation distance of infinity [77-78]. W_{12} can be obtained from the change of total potential energy ΔE_{p} per unit area during a separation simulation which involves no irreversible energy dissipation, as shown in Figure 6. The work of adhesion (i.e., 0.23 J/m^2) found in this way is close to the toughness (i.e., 0.26 J/m^2) of the untreated fibre-matrix interface, suggesting that the debonding of this interface involves little inelastic energy dissipation.

3.3. Debonding Process of Sizing-treated Fibre-Matrix Interface

Snapshots of the debonding process of the sizing-treated fibre-matrix interface at different displacements are shown in Figure 7. It is evident that the debonding process is quite different from that of the untreated fibre-matrix interface especially at the late stage with large displacements (see Figures 5 and 7). This is mainly due to the additional covalent bonds introduced by the silane coupling agent as the fibre sizing, as discussed in detail below.

Figure 8 shows the stress-displacement curve of the sizing-treated fibre-matrix interface and compares it with that of the untreated fibre-matrix interface. The stress-displacement behaviour of the two interfaces appears to be similar in the initial stage (Stage I in Figure 8), suggesting that the role of covalent bonds is insignificant at small displacements, as the polymer chains at the interface are still in the coiled state then [79]. The slight differences between the two curves in Stage I (Figure 8), including that in the peak stress, may be due to a number of factors including the difference in the nonbonding interactions caused by the sizing which changes the fibre surface as well as the slight difference in the cross-linking degree of the two models. The maximum stress is 274.6 MPa, and the tensile modulus was found to be 4.14 GPa based on the stress-displacement of the sizing-treated fibre-matrix interface.

By contrast, Figure 8 shows that the stress-displacement curves of the two models are significantly different after a displacement of around 1.5 nm (i.e., in Stage II). Different from the rapidly descending curve of the untreated fibre-matrix interface, the curve of the sizing-treated fibre-matrix interface is much longer with a sawtooth pattern and a large ultimate displacement (i.e., around 34 nm). As a result, the interfacial toughness of the latter (i.e., 2.85 J/m^2) is much larger than (over ten times) that of the former (i.e., 0.26 J/m^2). The above observations suggest that chemical bonds at the interface play an important role in Stage II. Because of the strong covalent bonds between the matrix and the sizing-treated fibre, the polymer chains initially connected to the fibre remain adhered to the fibre despite the increasing displacement, resulting in continuous slippage and tension, and thus increasing virial stresses of these chains. Consequently, the interface exhibits a hyperelastic behaviour, as also revealed by the previous studies (e.g., [80-81]); the extent of hyperelasticity depends on the density of connection achieved by covalent bonds (i.e., the coverage degree of the sizing) at the interface. With further increase of the displacement, the chemical bonds in some of the polymer chains may break, and the sawtooth pattern of the second-stage curve is a result of the combined actions of the slippage/tension and the breakage of covalent bonds of the chains. Figure 9 shows typical snapshots of the breakage of covalent bond and the slippage of polymer chains. The above process continues with the increase of displacement until the stress is zero when all connections are broken.

By comparing these mechanical parameters of the two models, it is evident that the fibre sizing leads to a significant increase in the interfacial toughness while has little effect on the peak interfacial stress, suggesting that the latter depends mainly on nonbonding interactions (i.e., van der Waals interactions and hydrogen bonds) while the former depends significantly on the chemical bonds. It may also be noted that the fibre sizing has a significant effect on the debonded interface. The fibre surface of the sizing-treated model after debonding has many residual polymers, molecules, and free radicals (Figure 7h), while the untreated fibre surface is relatively clean after debonding (Figure 5e). In addition, a significant number of relatively high ridges are formed on the surface of the sizing-treated fibre and the corresponding matrix after debonding, while the debonded fibre-matrix interface without sizing is relatively smooth, as shown in Figure 10. The above observations from the MD simulations is consistent with those reported by many experimental studies (e.g., [47, 82]).

3.4. Mechanochemical Process in Debonding Simulations

When a fibre-matrix interface is under tension, the tensile stress deforms chemical bonds, reduces the energy needed to break chemical bonds, and thus increases the probability of thermal scission of the deformed bonds [83]. This mechanochemical process has seldom been investigated in the previous MD studies on fibre-matrix interfaces, as they mostly performed classical MD simulations which cannot simulate the breakage of chemical bonds. In the present study, the ReaxFF force field was adopted, which allows the mechanochemical process to be examined in the debonding simulations.

The chemical bond evolution in the debonding process of the two fibre-matrix interface models are evaluated by counting the covalent bonds since tension is applied to the interface. The cutoff lengths of various covalent bonds for counting are listed in Table 2. Three kinds of covalent bonds are involved in this process, namely, the C-O bonds (i.e., ether linkage), the O-H bonds and the N-H bonds. Among the three, the most critical bond is the C-O bond (ether linkage), which, as a covalent bond in the main chain, directly affects the chain connection or the chain length; the scission of ether linkages of the main chain was reported in the experimental degradation studies of epoxy resin [84-85].

The evolution of total covalent bonds and the C-O bonds is shown in Figures 11a and 11b, respectively, for the untreated fibre-matrix model, while the corresponding results for the sizing-treated fibre-matrix model are shown in Figures 11c and 11d. It is found that although there is no covalent bond between the untreated fibre and the matrix, 0.2% of the total covalent bonds and 3.25% of the C-O bonds inside the matrix are broken during the debonding process of the interface. For the sizing-treated fibre-matrix interface, the breakage of covalent bonds is more severe: nearly 0.4% of the total covalent bonds and 8.5% of C-O bonds are broken during the debonding process.

It should be noted that the mechanochemical process is an issue of great complexity, and is affected by many factors including the strain rate and the temperature. In addition, the process involves not only the breaking of chemical bonds but also the formation of new chemical bonds. A full understanding of the mechanochemical process in an FRP composite under various mechanical and environmental actions is of fundamental importance to clarify the deterioration mechanism of the composite. While this is beyond the scope of the present study, the MD simulation method with the ReaxFF reactive force field adopted here has been shown to be able to capture the mechanochemical phenomena as well as their effects on the mechanical properties of FRP composites. This simulation method therefore provides a potentially effective way to explore the deterioration mechanism of fibre-matrix interfaces.

4. CONCLUSIONS

This paper has presented a study on all-atom simulations of the debonding process of fibre-matrix interfaces with and without fibre sizing. Two models were constructed using the classical MD simulations with the CVFF, and periodic boundary conditions were applied along the interfaces; DGEBA and mPDA were used to model the polymer matrix, silica was used to model the glass fibre, while silane was used to model the fibre sizing. The ReaxFF were then used for the MD simulations of the debonding process of the two models, so that the breakage of chemical bonds in this process, which is particularly important for sizing-treated fibre-matrix interface, was appropriately simulated.

The method of constructing the two models has been shown to be valid and efficient, as demonstrated by the satisfactory degrees of cross-linking of the matrix in the models, as well as the fact that the simulated mass densities of the matrix are close to those reported in the previous experimental and theoretical studies on DGEBA/mPDA matrices.

The ReaxFF MD simulations have allowed the entire debonding process of the two interface models to be examined in terms of the stress-displacement curve, the fracture fibre/matrix surfaces, the interfacial mechanical properties and the mechanochemical interactions. The following conclusions can be obtained based on the results and discussions presented in the paper.

(1) The stress-displacement curve of the interface without fibre sizing possesses a rapidly descending branch after the peak stress. By contrast, the post-peak branch of the curve of the sizing-treated interface exhibits a sawtooth pattern and a much larger ultimate displacement. The sawtooth pattern of the curve is a result of the combined actions of the slippage/tension and the breakage of covalent bonds of the polymer chains which are adhered to the fibre surface.
(2) The sizing treatment with its resulting covalent bonds at the fibre-matrix interface appears to have little effect on the peak stress of the interface but significantly increases the interface toughness (i.e., by around 10 times). The much larger interface toughness of the sizing-treated interface is mainly due to the energy dissipated by breaking covalent bonds as well as the significantly enhanced local inelastic deformation induced by covalent bonds in the debonding process.
(3) After debonding, the fracture surfaces of the model without fibre sizing are relatively smooth and clean, while the fibre surface of the sizing-treated model has many residual polymers, molecules, and free radicals. In addition, a significant number of relatively high ridges are formed on the surface of the sizing-treated fibre and the corresponding matrix after debonding.
(4) The tension process of fibre-matrix interfaces increases the probability of thermal scission of covalent bonds. The breakage of covalent bonds was found to occur in the polymer matrix of the models with and without fibre sizing, but a significantly larger number of broken covalent bonds were observed in the former.

The conclusions from this study provide insights, at the atomic level, into the fundamental debonding mechanism of fibre-matrix interfaces with or without fibre sizing under tension. The characteristics of the fracture surfaces and the scission of C-O bonds (ether linkages) observed in the MD simulations are consistent with pervious experimental observations. Importantly, the modelling method developed and adopted in this study, with the reactive force field, has been demonstrated to be effective in simulating the mechanochemical process including the formation and breakage of covalent bonds under stresses. This method therefore opens up a new avenue of investigating the deterioration mechanism of FRP composites under combined mechanical-chemical-thermal actions (e.g., in marine environments).

It should be noted that this modelling method may also be used to generate fundamental thermodynamic and kinetic information for upscale modelling. With this information as the inputs, the evolution of complex interfaces and defects (e.g., cracks and voids) can be predicted by the phase field method. Such evolutionary patterns may be expressed by a probability function and be further used to predict the macroscopic mechanical and durability properties of the material/structure by a finite element method. By adopting the abovementioned multi-scale modelling approach, the micromechanisms of the effects of various issues/variables involved in the production process of FRP (e.g., graft coverage, curing degree, surface roughness) on its macroscopic properties can be clarified, which may be used to provide fundamental recommendations for the design and application of FRP in the construction and building industry.

ACKNOWLEDGEMENTS

The authors gratefully acknowledge the financial support provided by the Hong Kong Research Grants Council (Project No: T22-502/18-R).

Appendices

Appendix A. Total potential energy of classical MD simulation

The total potential energy considered in the classical MD simulation with the CVFF consists of two parts (i.e., the bond energy E_{bond} and the nonbond energy E_{nonbond}), as expressed by the following equation [57]:

$$\begin{aligned} E &= E_{\text{bond}} + E_{\text{nonbond}} \\ &= \sum_{\text{bonds}} k_{\text{b}} \left(l - l_0\right)^2 + \sum_{\text{angles}} k_{\text{a}} \left(\theta - \theta_0\right)^2 + \sum_{\text{torsion}} k_{\text{t}} \left[1 + \cos\left(n\phi - \phi_0\right)\right]. \\ &\quad + \sum_{\text{vdW}} 4\varepsilon_{\text{ij}} \left[\left(\frac{\sigma_{\text{ij}}}{r_{\text{ij}}}\right)^{12} - \left(\frac{\sigma_{\text{ij}}}{r_{\text{ij}}}\right)^{6}\right] + \sum k_{\text{e}} \frac{q_{\text{i}} q_{\text{j}}}{r_{\text{ij}}} \end{aligned} \tag{A1}$$

In Eq. A1, E_{bond} is the sum of the bond, angle and torsion energies. On the right side of Eq. A1, the first term represents the energy between covalently bonded atoms, where k_{b}, l and l_0 are the spring constant of the harmonic bond and the real and equilibrium bond distances, respectively; the second term represents the energy due to the geometry of electron orbitals involved in covalent bonding, where k_{a}, θ and θ_0 are the force constant of the angle bond and the real and equilibrium angles, respectively; the third term represents the energy of twisting a bond due to the bond order and neighboring bonds, where k_{t}, n, ϕ and ϕ_0 are the force constant, the periodicity, the dihedral angle and the factor phase, respectively. E_{nonbond} between two atoms i and j separated by r_{ij} is the sum of the Lennard-Jones (LJ) potential (the fourth term on the right side of Eq. A1) and the electrostatic potential energy (the last term on the right side of Eq. A1). Here, ε_{ij} is the depth of the LJ potential well; σ_{ij} is the zero-potential distance; k_{e} is the electrostatic constant; q_{i} and q_{j} are the charges of the corresponding atoms.

Appendix B. Total potential energy of ReaxFF MD simulation

The total potential energy considered in the ReaxFF force field has a more complicated form as follows [53]:

$$\begin{aligned} E = E_{\text{bond}} + E_{\text{lp}} + E_{\text{over}} + E_{\text{under}} + E_{\text{val}} + E_{\text{pen}} + E_{\text{coa}} \\ + E_{\text{tor}} + E_{\text{conj}} + E_{\text{Hbond}} + E_{\text{vdW}} + E_{\text{Coulomb}} \end{aligned} . \tag{B1}$$

The specific meaning and expression of each energy term in Eq. B1 can be found in the references [53]. All the above energy terms are functions of the bond order. The bond order BO_{ij} is defined as a function of the distance r_{ij} between atoms, and the definitions of single bond BO_{ij}^{σ}, double bond BO_{ij}^{π}, and triple bond $BO_{\text{ij}}^{\pi\pi}$ in chemistry are used to divide the bond order into three parts of chemical significance [53]:

$$BO_{\text{ij}} = BO_{\text{ij}}^{\sigma} + BO_{\text{ij}}^{\pi} + BO_{\text{ij}}^{\pi\pi} . \tag{B2}$$

Appendix C. Virial stress tensor of an atom

The virial stress tensor of an atom is shown as follows [72]:

$$\boldsymbol{\sigma} = \frac{1}{\Omega}\left\langle -\sum_{\alpha} m_{\alpha} \boldsymbol{v}_{\alpha} \otimes \boldsymbol{v}_{\alpha} + \frac{1}{2} \sum_{\alpha,\beta\neq\alpha} \boldsymbol{r}_{\alpha\beta} \otimes \boldsymbol{f}_{\alpha\beta} \right\rangle, \tag{C1}$$

where Ω is the volume of the selected observation space; m_{α} and $\boldsymbol{v}_{\alpha}$ are the mass and velocity of atom α, respectively; $\boldsymbol{r}_{\alpha\beta}$ is the position vector from atom α to atom β; and $\boldsymbol{f}_{\alpha\beta}$ is the force of atom β on atom α in the conservative system.

REFERENCES

[1] Teng JG, Chen JF, Smith ST, Lam L. FRP-strengthened RC structures. Wiley: New York; 2002.

[2] Hollaway L. A review of the present and future utilisation of FRP composites in the civil infrastructure with reference to their important in-service properties. Constr Build Mater 2010; 24: 2419-2445.

[3] Buyukozturk O, Gunes O, Karaca E. Progress on understanding debonding problems in reinforced concrete and steel members strengthened using FRP composites. Constr Build Mater 2004; 18: 9-19.

[4] Teng JG, Yuan H, Chen JF. FRP-to-concrete interfaces between two adjacent cracks: Theoretical model for debonding failure. Int J Solids Struct 2006; 43: 5750-5778.

[5] Yu T, Fernando D, Teng JG, Zhao XL. Experimental study on CFRP-to-steel bonded interfaces. Compos B Eng 2012; 43: 2279-2289.

[6] Yu T, Zhang B, Cao YB, Teng JG. Behavior of hybrid FRP-concrete-steel double-skin tubular columns subjected to cyclic axial compression. Thin Wall Struct 2012; 61: 196-203.

[7] Zhang SS, Yu T, Chen GM. Reinforced concrete beams strengthened in flexure with near-surface mounted (NSM) CFRP strips: Current status and research needs. Compos B Eng 2017; 131: 30-42.

[8] Zeng JJ, Duan ZJ, Guo YC, Xie ZH, Li LJ. Novel fiber-reinforced polymer cross wrapping strengthening technique: A comparative study. Adv Struct Eng 2020; 23: 979-996.

[9] Foraboschi P. Effectiveness of novel methods to increase the FRP-masonry bond capacity. Compos B Eng 2016; 107: 214-232.

[10] Bank LC. Composites for construction: structural design with FRP materials. John Wiley & Sons: Hoboken; 2006.

[11] Teng JG, Yu T, Wong YL, Dong SL. Hybrid FRP–concrete–steel tubular columns: Concept and behavior. Constr Build Mater 2007; 21: 846-854.

[12] Yu T, Zhao H, Ren T, Remennikov A. Novel hybrid FRP tubular columns with large deformation capacity: Concept and behaviour. Compos Struct 2019; 212: 500-512.

[13] Zhang B, Yu T, Teng JG. Behavior and modelling of FRP-concrete-steel hybrid double-skin tubular columns under repeated unloading/reloading cycles. Compos Struct 2021; 258: 113393.

[14] Zhang B, Zhao JL, Huang T, Zhang NY, Zhang YJ, Hu XM. Effect of fiber angles on hybrid fiber-reinforced polymer–concrete–steel double-skin tubular columns under monotonic axial compression. Adv Struct Eng 2020; 23: 1487-1504.

[15] Zhao J, Xu C, Sun L, Wu D. Behaviour of FRP-confined compound concrete–filled circular thin steel tubes under axial compression. Adv Struct Eng 2020; 23: 1772-1784.

[16] Sousa JM, Correia JR, Cabral-Fonseca S, Diogo AC. Effects of thermal cycles on the mechanical response of pultruded GFRP profiles used in civil engineering applications. Compos Struct 2014; 116: 720-731.

[17] Sun P, Zhao Y, Luo Y, Sun L. Effect of temperature and cyclic hygrothermal aging on the interlaminar shear strength of carbon fiber/bismaleimide (BMI) composite. Mater Des 2011; 32: 4341-4347.

[18] Azwa Z, Yousif B, Manalo A, Karunasena W. A review on the degradability of polymeric composites based on natural fibres. Mater Des 2013; 47: 424-442.

[19] Grammatikos SA, Jones RG, Evernden M, Correia JR. Thermal cycling effects on the durability of a pultruded GFRP material for off-shore civil engineering structures. Compos Struct 2016; 153: 297-310.

[20] Selzer R, Friedrich K. Mechanical properties and failure behaviour of carbon fibre-reinforced polymer composites under the influence of moisture. Compos Part A-Appl S 1997; 28: 595-604.

[21] Silva MAG, da Fonseca BS, Biscaia H. On estimates of durability of FRP based on accelerated tests. Compos Struct 2014; 116: 377-387.

[22] Lu C, Yang Y, He L. Mechanical and durability properties of GFRP bars exposed to aggressive solution environments. Sci Eng Compos Mater 2021; 28: 11-23.

[23] Micelli F, Myers JJ. Durability of FRP-confined concrete. Proc Instit Civ Eng-Constr Mater 2008; 161: 173-185.

[24] Aiello MA, Ombres L. Environmental Effects on the Mechanical Properties of Glass-FRP and Aramid-FRP Rebars. Mech Compos Mater 2000; 36: 395-398.

[25] Laoubi K, El-Salakawy E, Benmokrane B. Creep and durability of sand-coated glass FRP bars in concrete elements under freeze/thaw cycling and sustained loads. Cem Concr Compos 2006; 28: 869-878.

[26] Foraboschi P. Predictive multiscale model of delayed debonding for concrete members with adhesively bonded external reinforcement. Compos: Mech, Comput, Appl 2012; 3: 307-329.

[27] Foraboschi P. Analytical model to predict the lifetime of concrete members externally reinforced with FRP. Theor Appl Fract Mech 2015; 75: 137-145.

[28] Chen L, Chai S, Liu K, Ning N, Gao J, Liu Q, Chen F, Fu Q. Enhanced Epoxy/Silica Composites Mechanical Properties by Introducing Graphene Oxide to the Interface. ACS Appl Mater Interfaces 2012; 4: 4398-4404.

[29] Benmokrane B, Ali AH, Mohamed HM, ElSafty A, Manalo A. Laboratory assessment and durability performance of vinyl-ester, polyester, and epoxy glass-FRP bars for concrete structures. Compos B Eng 2017; 114: 163-174.

[30] Mourad AHI, Abdel Magid BM, El Maaddawy T, Grami ME. Effect of Seawater and Warm Environment on Glass/Epoxy and Glass/Polyurethane Composites. Appl Compos Mater 2010; 17: 557-573.

[31] Wang Z, Zhao XL, Xian G, Wu G, Singh Raman RK, Al Saadi S, Haque A. Long-term durability of basalt- and glass-fibre reinforced polymer (BFRP/GFRP) bars in seawater and sea sand concrete environment. Constr Build Mater 2017; 139: 467-489.

[32] Tatar J, Brenkus NR, Subhash G, Taylor CR, Hamilton HR. Characterization of adhesive interphase between epoxy and cement paste via Raman spectroscopy and mercury intrusion porosimetry. Cem Concr Compos 2018; 88: 187-199.

[33] Chen L, Jin H, Xu Z, Shan M, Tian X, Yang C, Wang Z, Cheng B. A design of gradient interphase reinforced by silanized graphene oxide and its effect on carbon fiber/epoxy interface. Mater Chem Phys 2014; 145: 186-196.

[34] Lau D, Broderick K, Buehler MJ, Büyüköztürk O. A robust nanoscale experimental quantification of fracture energy in a bilayer material system. Proc Natl Acad Sci USA 2014; 111: 11990.

[35] Tam L-h, Lau D. Moisture effect on the mechanical and interfacial properties of epoxy-bonded material system: An atomistic and experimental investigation. Polymer 2015; 57: 132-142.

[36] Zhou A, Tam L-h, Yu Z, Lau D. Effect of moisture on the mechanical properties of CFRP–wood composite: An experimental and atomistic investigation. Compos B Eng 2015; 71: 63-73.

[37] Yaphary YL, Yu Z, Lam RHW, Hui D, Lau D. Molecular dynamics simulations on adhesion of epoxy-silica interface in salt environment. Compos B Eng 2017; 131: 165-172.

[38] Tam L-h, Chow CL, Lau D. Moisture effect on interfacial integrity of epoxy-bonded system: a hierarchical approach. Nanotechnology 2017; 29: 024001.

[39] Xiao Y, Xian G. Effects of moisture ingress on the bond between carbon fiber and epoxy resin investigated with molecular dynamics simulation. Polym Compos 2018; 39: E2074-E2083.

[40] Tam L-h, He L, Wu C. Molecular dynamics study on the effect of salt environment on interfacial structure, stress, and adhesion of carbon fiber/epoxy interface. Compos Interfaces 2019; 26: 431-447.

[41] Wang XQ, Lau D. Atomistic investigation of GFRP composites under chloride environment. Adv Struct Eng 2020: 1369433220961749.

[42] Wang XQ, Jian W, Buyukozturk O, Leung CKY, Lau D. Degradation of epoxy/glass interface in hygrothermal environment: An atomistic investigation. Compos B Eng 2021; 206: 108534.

[43] Büyüköztürk O, Buehler MJ, Lau D, Tuakta C. Structural solution using molecular dynamics: Fundamentals and a case study of epoxy-silica interface. Int J Solids Struct 2011; 48: 2131-2140.

[44] Wang P, Yang Q, Wang M, Hou D, Jin Z, Wang P, Zhang J. Theoretical investigation of epoxy detachment from C-S-H interface under aggressive environment. Constr Build Mater 2020; 264: 120232.

[45] Jiang F, Yang Q, Wang Y, Wang P, Hou D, Jin Z. Insights on the adhesive properties and debonding mechanism of CFRP/concrete interface under sulfate environment: From experiments to molecular dynamics. Constr Build Mater 2021; 269: 121247.

[46] Iglesias J, González-Benito J, Aznar A, Bravo J, Baselga J. Effect of glass fiber surface treatments on mechanical strength of epoxy based composite materials. J Colloid Interface Sci 2002; 250: 251-260.

[47] Sever K, Sarikanat M, Seki Y, Tavman IH. Concentration effect of γ - glycidoxypropyltrimethoxysilane on the mechanical properties of glass fiber–epoxy composites. Polym Compos 2009; 30: 1251-1257.
[48] Zhao F, Huang Y. Grafting of polyhedral oligomeric silsesquioxanes on a carbon fiber surface: novel coupling agents for fiber/polymer matrix composites. J Mater Chem 2011; 21: 3695-3703.
[49] Luo H, Xiong G, Ma C, Chang P, Yao F, Zhu Y, Zhang C, Wan Y. Mechanical and thermo-mechanical behaviors of sizing-treated corn fiber/polylactide composites. Polym Test 2014; 39: 45-52.
[50] Zhang M, Jiang B, Chen C, Drummer D, Zhai Z. The Effect of Temperature and Strain Rate on the Interfacial Behavior of Glass Fiber Reinforced Polypropylene Composites: A Molecular Dynamics Study. Polymers 2019; 11: 1766.
[51] Brenner DW, Shenderova OA, Harrison JA, Stuart SJ, Ni B, Sinnott SB. A second-generation reactive empirical bond order (REBO) potential energy expression for hydrocarbons. J Phys: Condens Matter 2002; 14: 783-802.
[52] Stuart SJ, Tutein AB, Harrison JA. A reactive potential for hydrocarbons with intermolecular interactions. J Chem Phys 2000; 112: 6472-6486.
[53] van Duin ACT, Dasgupta S, Lorant F, Goddard WA. ReaxFF: A reactive force field for hydrocarbons. J Phys Chem A 2001; 105: 9396-9409.
[54] Plimpton S. Fast parallel algorithms for short-range molecular dynamics. J Comput Phys 1995; 117: 1-19.
[55] Tam L-h, Lau D. A molecular dynamics investigation on the cross-linking and physical properties of epoxy-based materials. RSC Adv. 2014; 4: 33074-33081.
[56] Wu C, Xu W. Atomistic molecular modelling of crosslinked epoxy resin. Polymer 2006; 47: 6004-6009.
[57] Dauber Osguthorpe P, Roberts VA, Osguthorpe DJ, Wolff J, Genest M, Hagler AT. Structure and energetics of ligand binding to proteins: Escherichia coli dihydrofolate reductase - trimethoprim, a drug - receptor system. Proteins Struct Funct Bioinf 1988; 4: 31-47.
[58] Unger R, Braun U, Fankhänel J, Daum B, Arash B, Rolfes R. Molecular modelling of epoxy resin crosslinking experimentally validated by near-infrared spectroscopy. Comp Mater Sci 2019; 161: 223-235.
[59] Steinbach PJ, Brooks BR. New spherical - cutoff methods for long - range forces in macromolecular simulation. J Comput Chem 1994; 15: 667-683.
[60] Zhang M, Matinlinna JP. E-glass fiber reinforced composites in dental applications. Silicon 2012; 4: 73-78.
[61] Jesionowski T, Krysztafkiewicz A. Influence of silane coupling agents on surface properties of precipitated silicas. Appl Surf Sci 2001; 172: 18-32.
[62] Howarter JA, Youngblood JP. Optimization of Silica Silanization by 3-Aminopropyltriethoxysilane. Langmuir 2006; 22: 11142-11147.

[63] Gauthier S, Aimé JP, Bouhacina T, Attias AJ, Desbat B. Study of Grafted Silane Molecules on Silica Surface with an Atomic Force Microscope. Langmuir 1996; 12: 5126-5137.

[64] Dugas V, Chevalier Y. Surface hydroxylation and silane grafting on fumed and thermal silica. J Colloid Interface Sci 2003; 264: 354-361.

[65] Chen WY, Wang YZ, Kuo SW, Huang CF, Tung PH, Chang FC. Thermal and dielectric properties and curing kinetics of nanomaterials formed from poss-epoxy and meta-phenylenediamine. Polymer 2004; 45: 6897-6908.

[66] Gupta V, Drzal L, Lee CC, Rich M. The temperature - dependence of some mechanical properties of a cured epoxy resin system. Polym Eng Sci 1985; 25: 812-823.

[67] Downey MA, Drzal LT. Toughening of carbon fiber-reinforced epoxy polymer composites utilizing fiber surface treatment and sizing. Compos Part A-Appl S 2016; 90: 687-698.

[68] Li Y, Wang S, Wang Q. A molecular dynamics simulation study on enhancement of mechanical and tribological properties of polymer composites by introduction of graphene. Carbon 2017; 111: 538-545.

[69] Nosé S. A molecular dynamics method for simulations in the canonical ensemble. Mol Phys 1984; 52: 255-268.

[70] Hoover WG. Canonical dynamics: Equilibrium phase-space distributions. Phys Rev A 1985; 31: 1695.

[71] Bai C, Liu L, Sun H. Molecular dynamics simulations of methanol to olefin reactions in HZSM-5 zeolite using a ReaxFF force field. J Phys Chem C 2012; 116: 7029-7039.

[72] Subramaniyan AK, Sun CT. Continuum interpretation of virial stress in molecular simulations. Int J Solids Struct 2008; 45: 4340-4346.

[73] Zhao Y-P. Some new mesoscopic crossover length scales concerning the Hamaker constant. Sci China Technol Sci 2019; 62: 2310-2312.

[74] France Lanord A, Rigby D, Mavromaras A, Eyert V, Saxe P, Freeman C, Wimmer E In *MedeA®: Atomistic simulations for designing and testing materials for micro/nano electronics systems*, 2014 15th International Conference on Thermal, Mechanical and Mulit-Physics Simulation and Experiments in Microelectronics and Microsystems (EuroSimE), IEEE: 2014; pp 1-8.

[75] Rao V, Drzal LT. The dependence of interfacial shear strength on matrix and interphase properties. Polym Compos 1991; 12: 48-56.

[76] Kreahling R, Kline D. Thermal conductivity, specific heat, and dynamic mechanical behavior of diglycidyl ether of bisphenol a cured with m-phenylenediamine. J Appl Polym Sci 1969; 13: 2411-2425.

[77] Dupré A, Dupré P. Théorie mécanique de la chaleur. Gauthier-Villars: 1869.

[78] Ebnesajjad S, Landrock AH. Adhesives technology handbook. William Andrew: 2014.

[79] Fisher TE, Marszalek PE, Fernandez JM. Stretching single molecules into novel conformations using the atomic force microscope. Nat Struct Biol 2000; 7: 719-724.

[80] Bouvard JL, Francis DK, Tschopp MA, Marin E, Bammann D, Horstemeyer M. An internal state variable material model for predicting the time, thermomechanical, and stress state dependence of amorphous glassy polymers under large deformation. Int J Plast 2013; 42: 168-193.

[81] Bouvard JL, Ward DK, Hossain D, Marin EB, Bammann DJ, Horstemeyer MF. A general inelastic internal state variable model for amorphous glassy polymers. Acta Mech 2010; 213: 71-96.

[82] Mohd Ishak ZA, Ariffin A, Senawi R. Effects of hygrothermal aging and a silane coupling agent on the tensile properties of injection molded short glass fiber reinforced poly(butylene terephthalate) composites. Eur Polym J 2001; 37: 1635-1647.

[83] Zhurkov SN. Kinetic concept of the strength of solids. Int J Fracture Mech 1965; 1: 311-323.

[84] Lin MS, Wang MW, Lee CT, Shao SY. Accelerated ageing behavior of compatible IPNs based on epoxy and methacrylated epoxy resins. Polym Degrad Stab 1998; 60: 505-510.

[85] Yan H, Lu CX, Jing DQ, Hou XL. Chemical degradation of amine-cured DGEBA epoxy resin in supercritical 1-propanol for recycling carbon fiber from composites. Chin J Polym Sci 2014; 32: 1550-1563.

Table 1. Material properties of DGEBA/mPDA at approximately 300 K

DGEBA/mPDA	Density (g/cm^3)	Tensile Modulus (GPa)	Cross-link Degree/Curing Conditions	Method
This study	1.29	4.34	73.9%	ReaxFF MD
Ref. [44]	1.17	2.83	80.0%	MD (COMPASS)
Ref. [74]	–	3.92	80.0%	MD (PCFF+)
Ref. [65]	1.34/1.38	–	~100%	Experiment/ Theoretical analysis
Ref. [66]	1.21 ~ 1.22	3.55 ~ 4.75	–	Experiment
Ref. [67]	1.20	–	–	Experiment
Ref. [75]	–	3.30	348 K-2 HR, 398 K-2 HR	Experiment
Ref. [76]	–	3.60 ~ 4.02	345 K-24 HR, 400 K-24 HR	Experiment

Table 2. Cutoff lengths of different covalent bonds for counting

Bond Type	Cutoff length (Å)
C-C	1.80
C-H	1.40
C-N	1.65
C-O	1.70
C-Si	1.85
N-H	1.45
O-H	1.20
O-Si	1.80

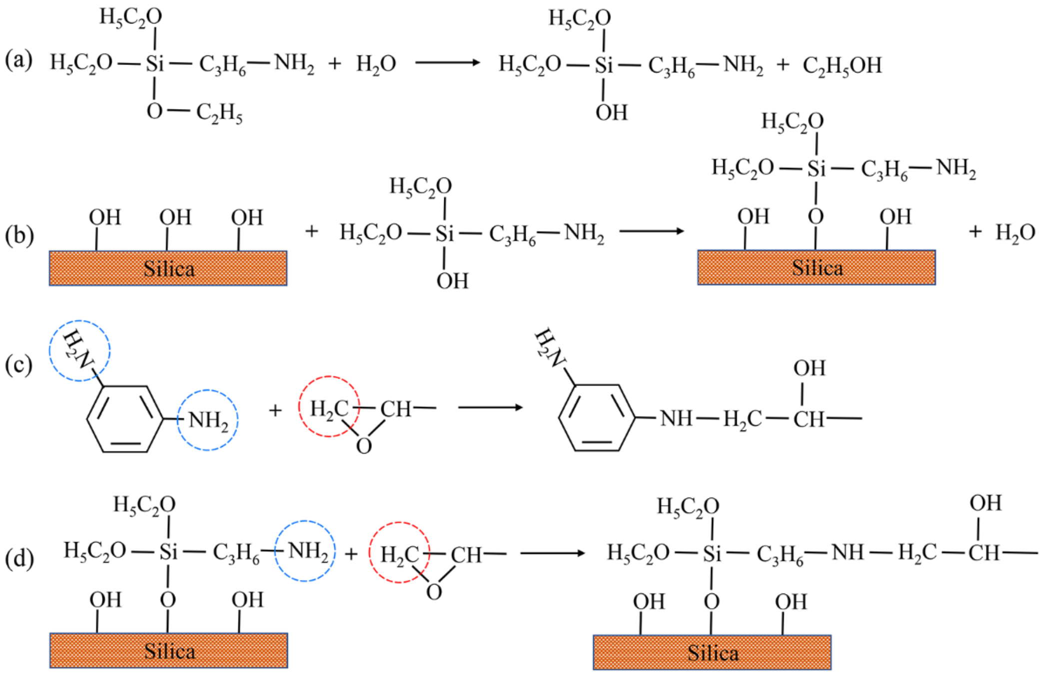

Figure 1. Schematics of chemical reactions: (a) silane hydrolyzing; (b) grafting procedure of hydroxylated glass fibers; (c) curing procedure between epoxy and curing agent; and (d) curing procedure between epoxy and grafted glass fibers.

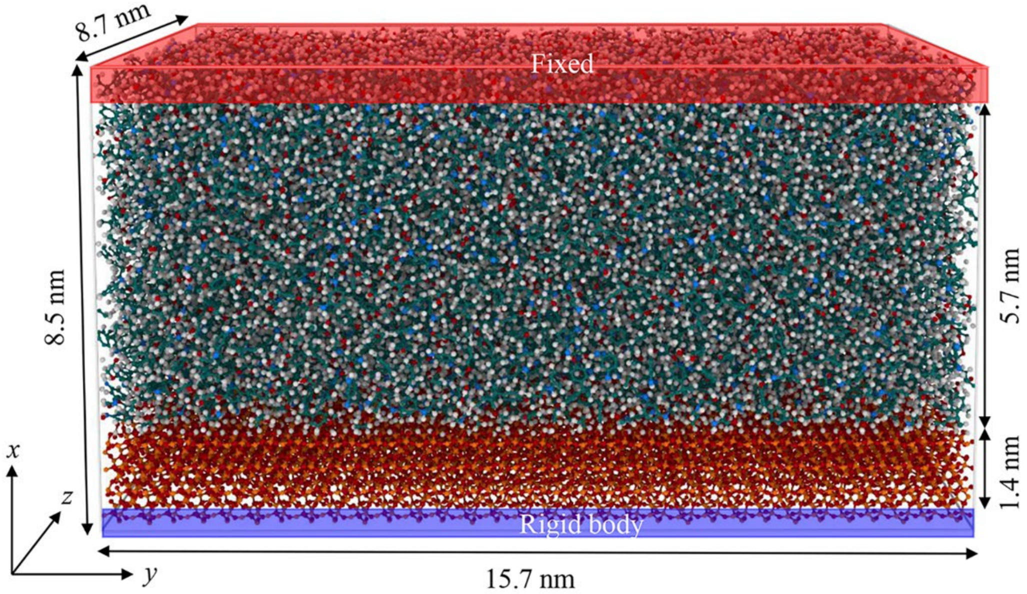

Figure 2. Initial MD model before tension process

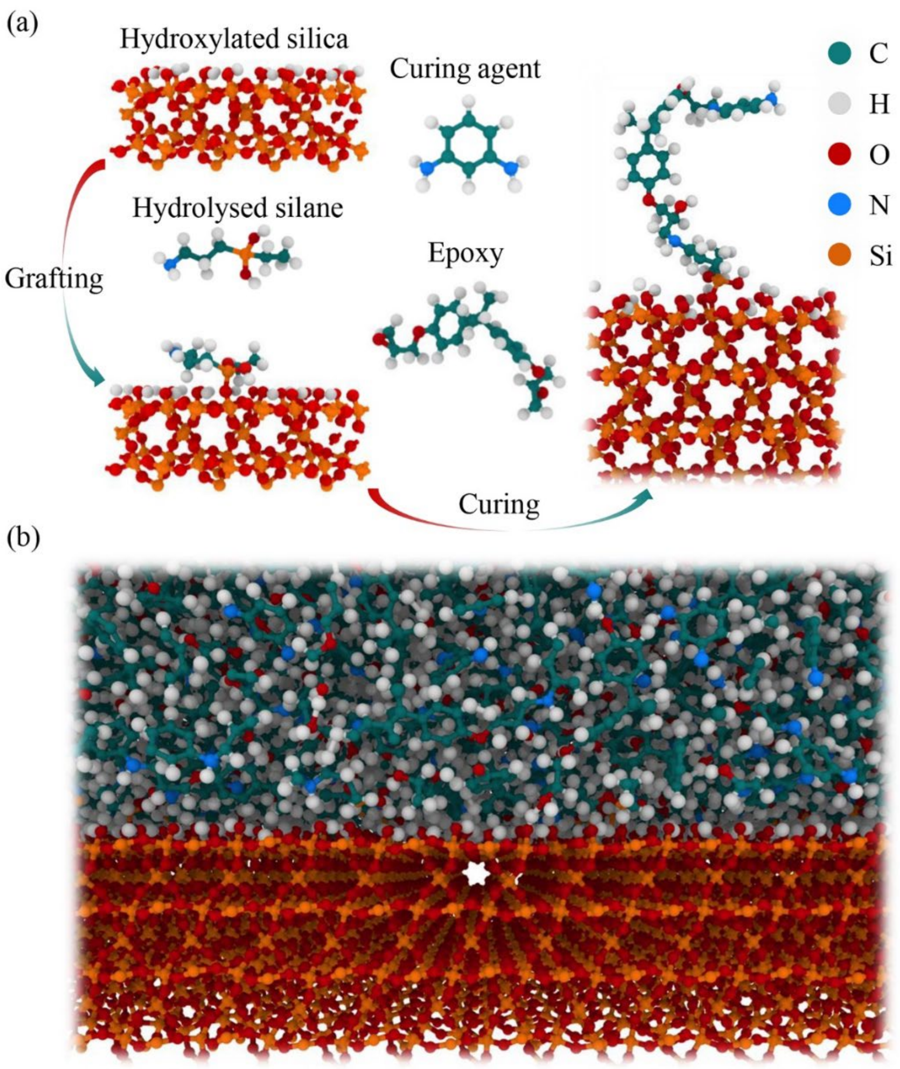

Figure 3. All-atom modeling process: (a) grafting and curing; (b) snapshot of part of the sizing-treated interface after curing

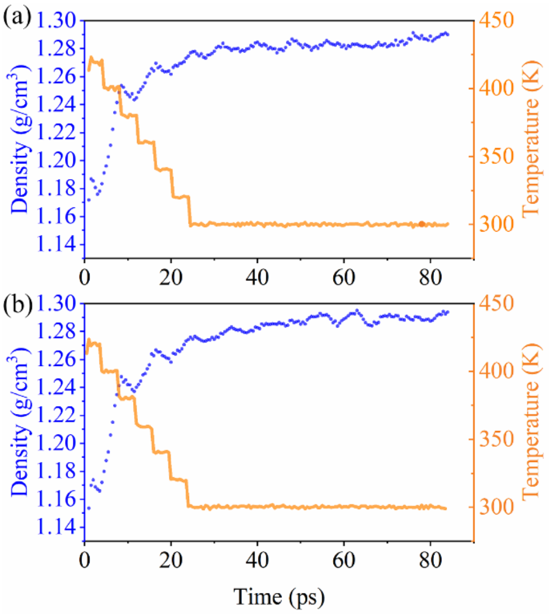

Figure 4. (a) Variation of temperature and density of the matrix in the relaxation process of the model with sizing treatment; (b) variation of temperature and density of the matrix in the relaxation process of the model without sizing treatment.

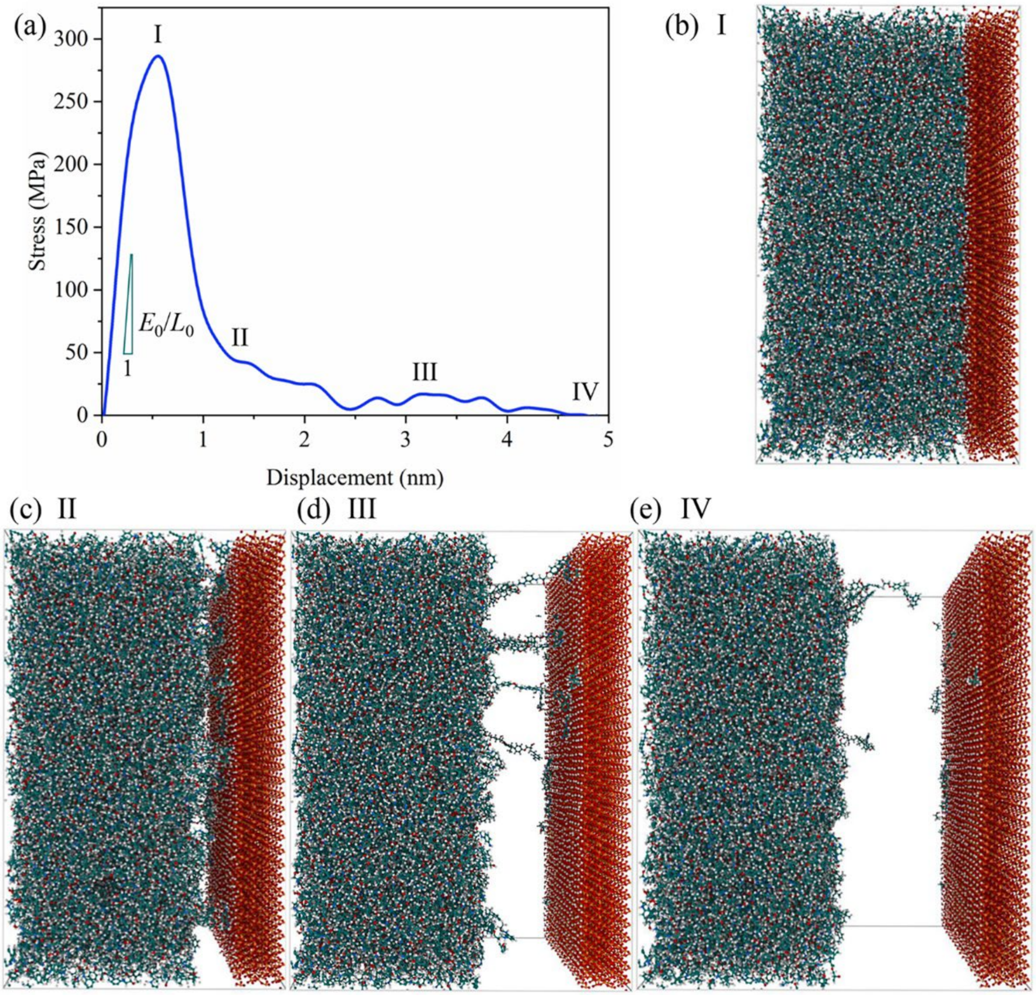

Figure 5. (a) Stress-displacement curve of the debonding process; and (b-e) snapshots of different states in the debonding process of the untreated fiber/matrix interface.

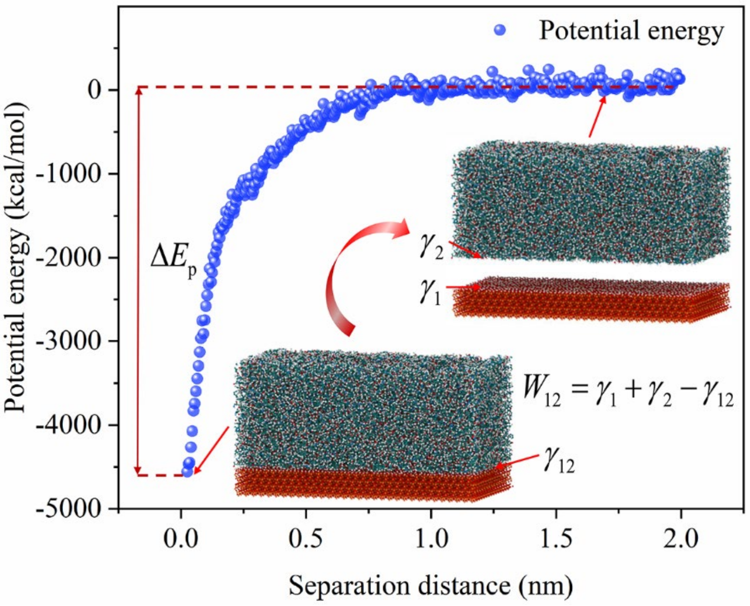

Figure 6. Evolution of potential energy in the separation of two surfaces Note: γ_1 and γ_2 are the surface energies of the two substances being bonded, respectively; γ_{12} is their interfacial energy.

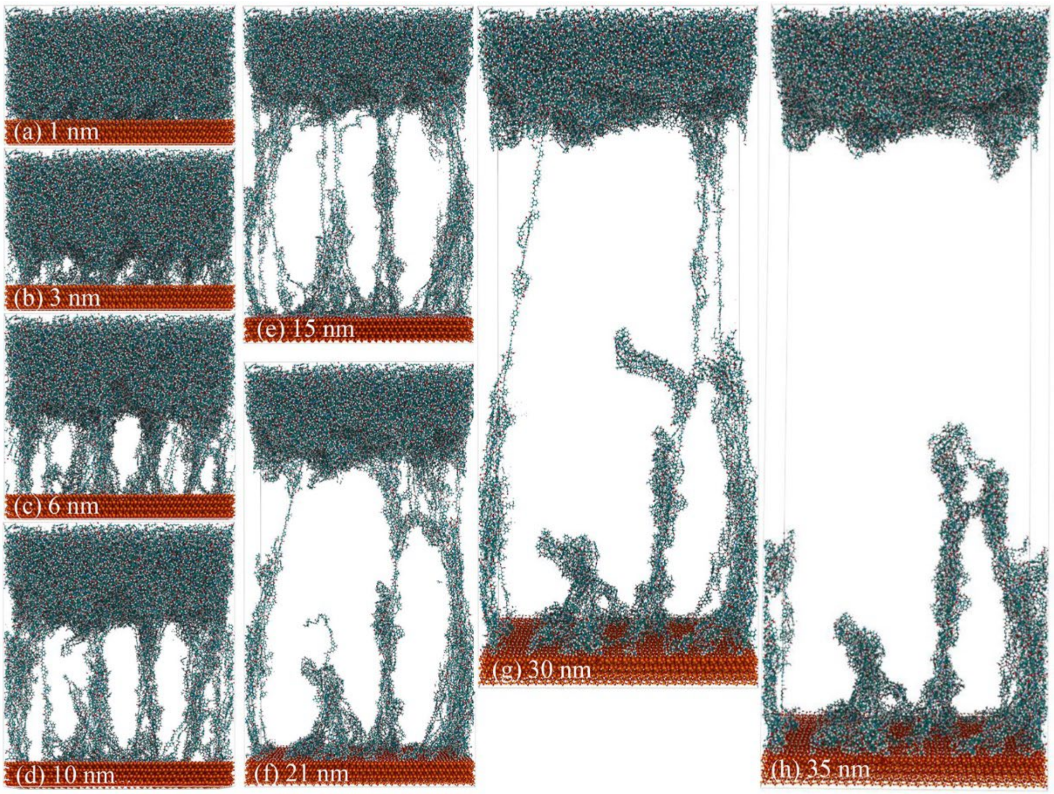

Figure 7. Snapshots of different states in the debonding process of the treated fiber/matrix interface: (a-h) Displacement from 1 nm to 35 nm.

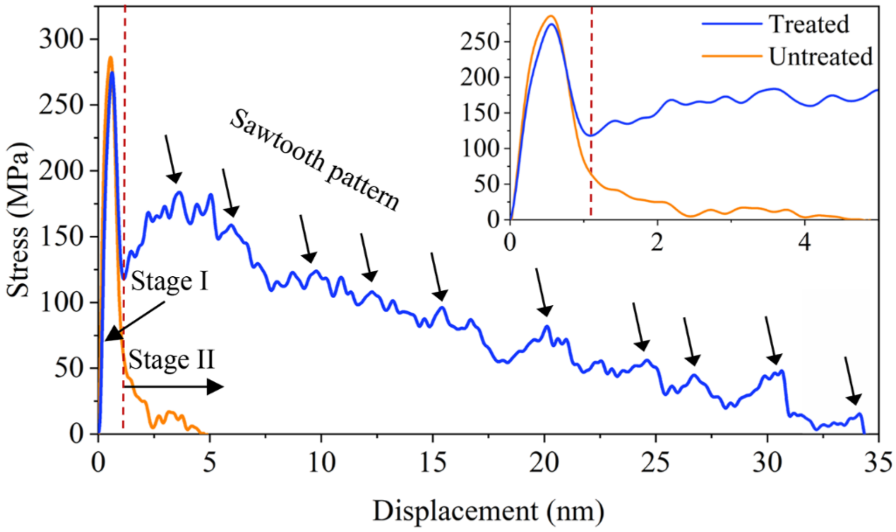

Figure 8. Stress-displacement curves of the debonding process

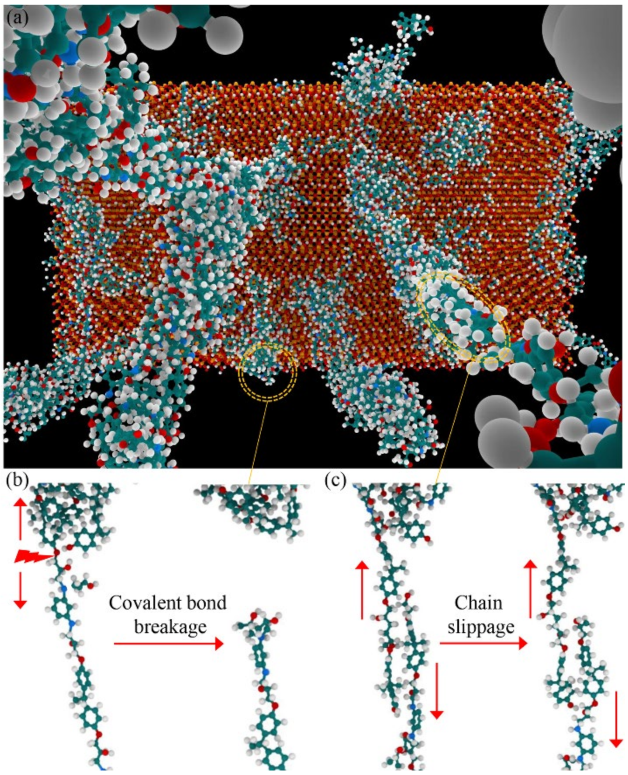

Figure 9. Polymer chains in the debonding process: (a) Inside perspective view of the connected chains between fiber and matrix; (b) Covalent bond breakage; (c) Chain slippage

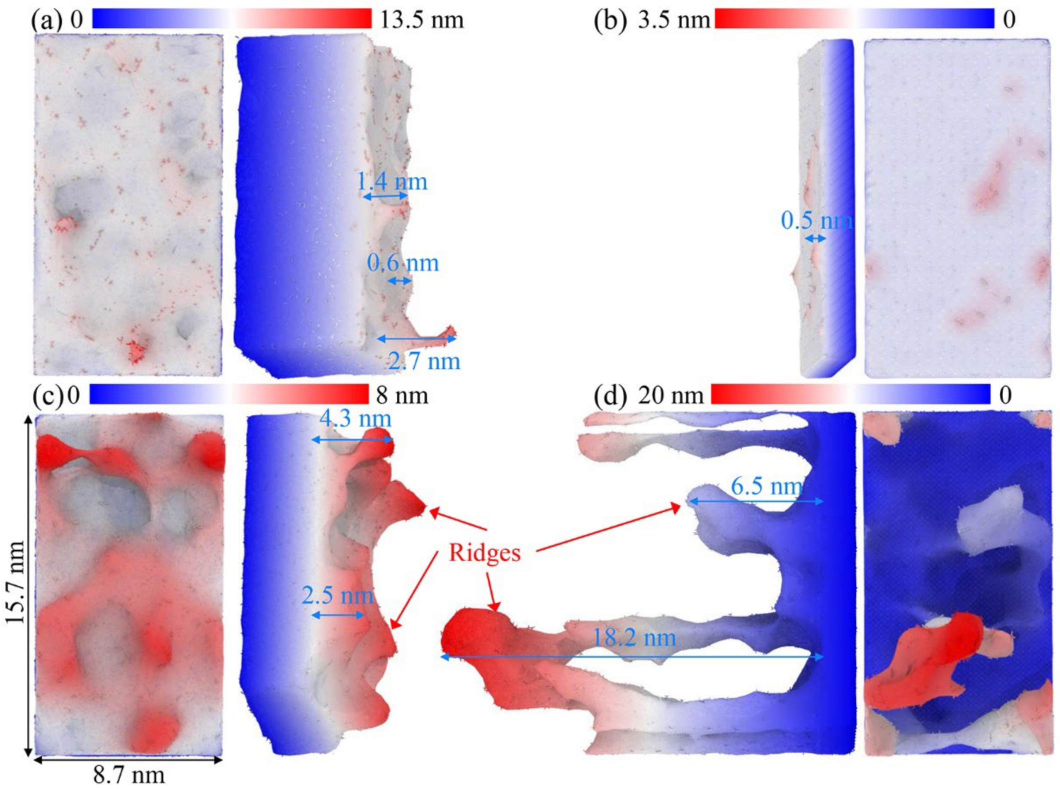

Figure 10. Fracture surfaces of the two interface models: (a-b) The untreated fiber/matrix interface: (a) top view (left) and side view (right) of fracture surface of the matrix; (b) side view (left) and top view (right) of fracture surface of the fiber. (c-d) The treated fiber/matrix interface: (a) top view (left) and side view (right) of fracture surface of the matrix; (b) side view (left) and top view (right) of fracture surface of the fiber

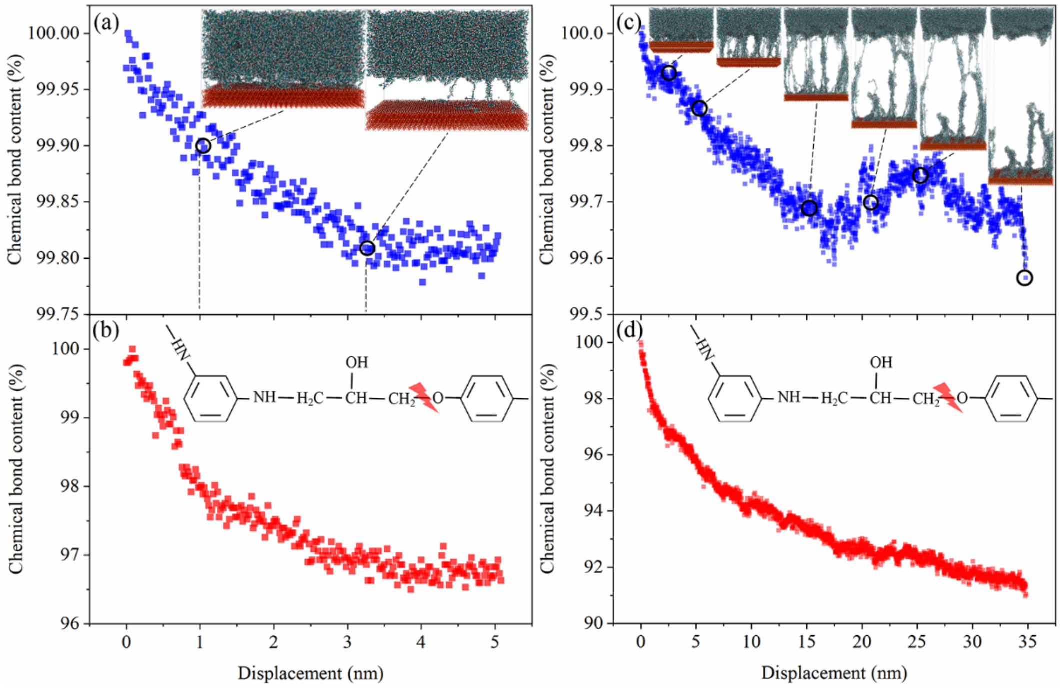

Figure 11. Evolution of chemical bonds in the debonding process of the two models: Total covalent bonds (a) and C-O bonds (ether linkage) (b) of the untreated model; Total covalent bonds (c) and C-O bonds (ether linkage) (d) of the treated model.